

# DV-3DLANE: END-TO-END MULTI-MODAL 3D LANE DETECTION WITH DUAL-VIEW REPRESENTATION

Yueru Luo<sup>1,2</sup>, Shuguang Cui<sup>2,1</sup>, Zhen Li<sup>2,1,✉</sup>

<sup>1</sup> FNii, CUHK-Shenzhen <sup>2</sup> School of Science and Engineering, CUHK-Shenzhen  
{222010057@link., shuguangcui@, lizhen@}{cuhk.edu.cn}

## ABSTRACT

Accurate 3D lane estimation is crucial for ensuring safety in autonomous driving. However, prevailing monocular techniques suffer from depth loss and lighting variations, hampering accurate 3D lane detection. In contrast, LiDAR points offer geometric cues and enable precise localization. In this paper, we present DV-3DLane, a novel end-to-end **Dual-View** multi-modal **3D Lane** detection framework that synergizes the strengths of both images and LiDAR points. We propose to learn multi-modal features in dual-view spaces, *i.e.*, *perspective view* (PV) and *bird's-eye-view* (BEV), effectively leveraging the modal-specific information. To achieve this, we introduce three designs: **1)** A bidirectional feature fusion strategy that integrates multi-modal features into each view space, exploiting their unique strengths. **2)** A unified query generation approach that leverages lane-aware knowledge from both PV and BEV spaces to generate queries. **3)** A 3D dual-view deformable attention mechanism, which aggregates discriminative features from both PV and BEV spaces into queries for accurate 3D lane detection. Extensive experiments on the public benchmark, OpenLane, demonstrate the efficacy and efficiency of DV-3DLane. It achieves state-of-the-art performance, with a remarkable **11.2** gain in F1 score and a substantial **53.5%** reduction in errors. The code is available at <https://github.com/JMoonr/dv-3dlane>.

## 1 INTRODUCTION

Autonomous driving (AD) technology in recent years has made remarkable strides, bringing us closer to the realization of fully self-driving vehicles. Within this field, one of the key challenges is the accurate detection of 3D lanes, a critical component for ensuring safe and reliable navigation. 3D lane detection entails identifying the 3D positions of lane boundaries in the environment, providing essential data for tasks like path planning and vehicle control.

3D lane detection is proposed to mitigate the limitations posed by the absence of depth information in 2D prediction. Currently, the majority of 3D lane detection methods rely on vision-centric approaches, *i.e.*, monocular solutions, where some designs are naturally borrowed and benefit from advances in 2D lane methods. Taking the perspective-view (PV) image as input, these monocular methods mainly utilize the inverse perspective mapping (IPM) Mallot et al. (1991) technique to warp the PV features into BEV. However, there are misalignment issues in the IPM-based methods when encountering non-flat roads, due to the rigid flat assumption of IPM Nedevschi et al. (2004); Yan et al. (2022). While some recent efforts have been made to address this issue and

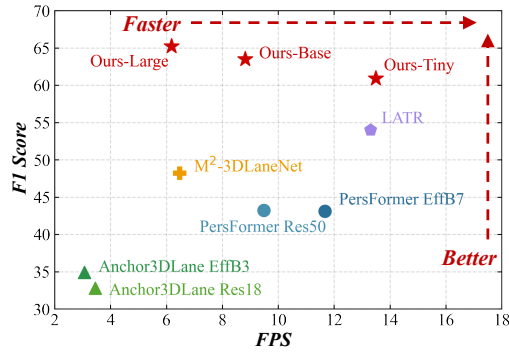


Figure 1: **FPS vs. F1 score.** All models are tested on a single V100 GPU, and F1-score is evaluated with a harsh distance threshold of **0.5m** on the OpenLane-1K dataset. Our model sets a new state-of-the-art, and our tiny version surpasses all previous methods with the fastest FPS. More details can be found in Table 1 and the Appendix.

<sup>✉</sup> Corresponding author.

have shown promising results by directly predicting 3D lanes in PV Bai et al. (2022b); Huang et al. (2023); Luo et al. (2023), these monocular 3D approaches, as vision-centric solutions, inevitably get stuck in capturing the complexity of real-world driving scenarios, when encountering adverse weather and lighting conditions. In contrast, as an active sensor, LiDAR excels in spatial localization and 3D structure perception, complementing the capabilities of passive sensor cameras, and it gets more widely used thanks to hardware advancements. A bunch of recent works in 3D object detection have demonstrated the power of LiDARs Zhou & Tuzel (2018); Lang et al. (2019); Yin et al. (2021a) and multiple modalities Liang et al. (2019); Wang et al. (2021); Yang et al. (2022); Li et al. (2022b); Chen et al. (2023) in autonomous driving scenarios. Whereas, *fewer endeavors* Bai et al. (2018); Luo et al. (2022a) *have been made to exploit multi-modal strength for 3D lane detection*. Albeit using extra LiDAR data, M<sup>2</sup>-3DLane Luo et al. (2022a) failed to make full use of features in image space which is crucial to 3D lane performance. Besides, M<sup>2</sup>-3DLane employs a naive fusion to aggregate multi-modal features, resulting in inferior performance to the camera-only methods(*e.g.*, Luo et al. (2023)).

Given the rich semantics inherent in images and the accurate positional information afforded by the BEV representation Phlion & Fidler (2020); Li et al. (2022d), we strive to exploit the multi-modal features to enhance the performance of 3D lane detection. Existing methods tend to fuse two modalities into a *single* space Liang et al. (2022); Liu et al. (2023b), *e.g.*, BEV, for feature extraction and subsequent prediction. However, this approach constrains the model’s capacity to harness modality-specific features. We contend that features represented in *both PV space and BEV space bear significance*, facilitating improved representation learning. Motivated by the above observation, we introduce **DV-3DLane**, a novel end-to-end multi-modal 3D lane detection framework.

To maintain a dual-view space representation, we adopt a symmetric backbone consisting of a PV branch and a BEV branch to extract features in PV and BEV spaces, respectively. To leverage the merits of both images and points for comprehensive feature learning in each view, we design a *bidiirectional* feature fusion (BFF) strategy. Subsequently, to effectively facilitate query-based detection using the retained dual-view features, we devise a *unified* query generator (UQG). This generator initially produces two sets of lane-aware queries: one from the PV space and the other from the BEV space. These two query sets are compelled to capture lane knowledge regarding semantics and spatiality, guided by auxiliary 2D segmentation supervision. Further, these two sets are then combined into a unified set that serves the decoder. To achieve the unification of dual-view queries, we propose a *lane-centric* clustering technique. Besides, we employ a Transformer decoder to aggressively integrate discriminative features from both views into the unified queries. For effective feature aggregation across different view spaces, we introduce a 3D dual-view deformable attention mechanism that considers the inherent properties of 3D space, resulting in deformed 3D sample points. These 3D sample points are then projected onto the PV and BEV planes, yielding 2D sample points in each respective view space. These projected 2D points are utilized for feature sampling within their respective view spaces.

In summary, our contributions are threefold :

- We introduce DV-3DLane, an end-to-end multi-modal 3D lane detection framework that harnesses the power of dual-view representation.
- We devise the BFF strategy to mutually fuse features across modalities, and design the UQG to merge lane-aware queries from dual views, yielding a unified query set. Further, a 3D dual-view deformation attention mechanism is introduced to aggregate dual-view features effectively.
- We conduct thorough experiments on the OpenLane benchmark to validate the effectiveness of our method. Experimental results show that DV-3DLane surpasses previous methods significantly, achieving an impressive **11.2-point** gain in F1 score and a remarkable **53.5% reduction** in errors (on average). Moreover, a 3D dual-view deformation attention mechanism is introduced to aggregate dual-view features effectively.

## 2 RELATED WORK

### 2.1 2D LANE DETECTION

Recent works in 2D lane detection can be broadly categorized into four main approaches: 1) Segmentation-based methods Lee et al. (2017); Pan et al. (2017); Neven et al. (2018); Hou et al.

(2019); Xu et al. (2020); Zheng et al. (2021) devote to classifying pixels into lanes or the background, necessitating further post-processing steps (*e.g.*, grouping and curve fitting) to produce lane instances. **2)** Anchor-based methods, inspired by region-based object detectors such as Faster-RCNN Ren et al. (2015), employ line-like anchors to localize lanes Wang et al. (2018); Li et al. (2019); Tabelini et al. (2021a). To overcome the limitations of straight-line constraints, Jin et al. (2022) employ eigenlane space to produce diverse lane shape candidates. **3)** Point-based methods Ko et al. (2021); Qu et al. (2021); Wang et al. (2022); Xu et al. (2022) attempt to flexibly localize key points along each lane instance and subsequently group the points belonging to the same lane. **4)** Parametric methods Van Gansbeke et al. (2019); Tabelini et al. (2021b); Liu et al. (2021); Feng et al. (2022) formulate lane detection as a curve fitting problem, leveraging prior knowledge about lane shapes by representing them using various parametric forms, such as polynomials and splines.

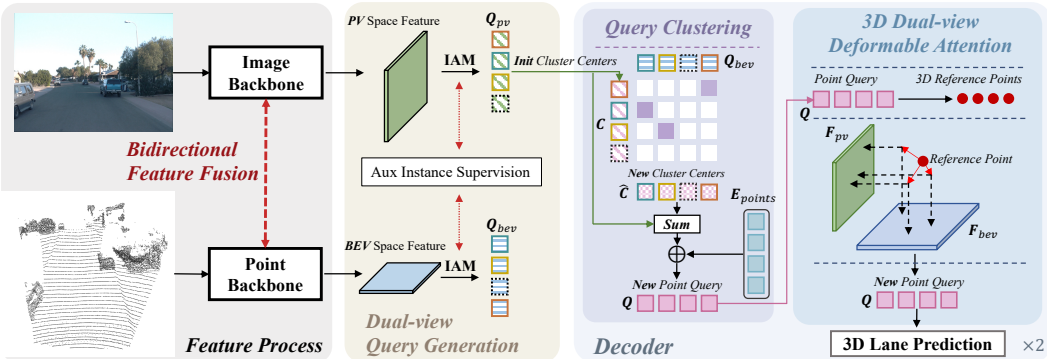


**Figure 2: Overview of DV-3DLane.** First, images and point clouds undergo separate processing by the image backbone and point backbone. In the middle stage of backbones, we introduce Bidirectional Feature Fusion (BFF) to fuse multi-modal features across views. Subsequently, the instance activation map (IAM) is utilized to produce lane-aware queries  $\mathbf{Q}_{pv}$  and  $\mathbf{Q}_{bev}$ . These queries are then subjected to Dual-view Query Clustering, which aggregates dual-view query sets  $\mathbf{Q}_{pv}$  and  $\mathbf{Q}_{bev}$  into a unified query set  $\mathbf{C}$ , further augmented with learnable point embeddings  $\mathbf{E}_{points}$  to form query  $\mathbf{Q}$ . Additionally, we introduce 3D Dual-view Deformable Attention to consistently aggregate point features from both view features  $\mathbf{F}_{pv}$  and  $\mathbf{F}_{bev}$  into  $\mathbf{Q}$ .  $\oplus$  denotes broadcast summation. Notably, the  $\oplus \mathbf{E}_{points}$  operation is performed only in the first layer, while in the following layer,  $\oplus \mathbf{Q}$  is utilized. Different colored boxes  $\square\square\square$  denote queries targeting different lanes; dashed boxes  $\square\square\square$  represent the background, and box texture indicates features.

## 2.2 3D LANE DETECTION

Existing methods center on vision-centric solutions and draw inspiration from the 2D task. Typically, monocular approaches Garnett et al. (2019); Efrat et al. (2020); Guo et al. (2020); Chen et al. (2022); Wang et al. (2023); Liu et al. (2022); Li et al. (2022a); Ai et al. (2023); Yao et al. (2023) construct surrogate representations using inverse perspective mapping (IPM), and perform predictions in this surrogate space. Nonetheless, due to its planar assumption, IPM inherently introduces discrepancies between the perspective and the surrogate view in non-flat areas. To address this limitation, recent efforts have endeavored to predict 3D lanes from the perspective view Yan et al. (2022); Bai et al. (2022b); Huang et al. (2023); Luo et al. (2023), or employ a depth-aware projection to enhance lane perception by incorporating LiDAR information Luo et al. (2022a).

## 2.3 MULTI-MODAL DETECTION

Despite advancements in lane detection, multi-modal methods remain relatively underexplored. Previous works typically utilize either BEV Bai et al. (2018); Yin et al. (2020); Luo et al. (2022a) or PV Zhang et al. (2021b) as representation spaces for performing 2D lane segmentation Yin et al. (2020); Zhang et al. (2021b) or 3D lane detection Bai et al. (2018); Luo et al. (2022a). For BEV-based methods, Bai et al. (2018) rasterizes LiDAR points to create a BEV image and transforms PV images into BEV using the estimated ground height derived from the LiDAR data. Similarly, M<sup>2</sup>-3DLane Luo et al. (2022a) utilizes the BEV space to fuse multi-modal features. To project PV features into BEV space, they lift compact 2D features into 3D space guided by the depth map and

further employ a pillar-based method Lang et al. (2019) to splat them into BEV. While these methods primarily focus on 3D tasks, Yin et al. (2020) leverages BEV space for fusing camera and LiDAR features, serving for 2D BEV lane segmentation. Conversely, Zhang et al. (2021b) adopts PV to fuse multi-modal features for 2D lane segmentation. In contrast to lane detection, multi-modal methods have been extensively studied in 3D object detection, with most previous multi-modal methods attempting to fuse image features into BEV space due to its compactness and interoperability for ambient perception Ma et al. (2022). These methods either adopt point-level fusion Sindagi et al. (2019); Wang et al. (2021); Yin et al. (2021b) to paint points, instance-level fusion to project 3D proposals to image space Yoo et al. (2020); Bai et al. (2022a), or feature-level fusion to transform features from PV space into BEV space Liu et al. (2023b); Liang et al. (2022). However, few works consider both the perspective view and BEV simultaneously.

### 3 METHODOLOGY

The overall framework of our DV-3DLane is depicted in Figure 2. Section 3.1 describes the bidirectional feature fusion module, which merges different modalities bidirectionally and constructs multi-modal features in both PV and BEV spaces. In Section 3.2, we present the unified query generator, which generates two lane-aware query sets from dual views and unifies them into a shared space in a lane-centric manner. Section 3.3 introduces the 3D dual-view deformable attention module, which effectively aggregates dual-view features into unified queries, serving for prediction.

#### 3.1 BIDIRECTIONAL FEATURE FUSION

Instead of merging different views into one single space Bai et al. (2018); Luo et al. (2022a); Liang et al. (2022); Li et al. (2022d); Liu et al. (2023b); Luo et al. (2024), we propose to retain features in both PV and BEV spaces while incorporating multi-modal features for each view. To achieve this, we employ a dual branch to extract features for each view, using images and points as input, respectively. Intermediately, we conduct *bidirectional* feature fusion between the symmetric branches to enhance each view with multiple modalities, as shown in Figure 3 and summarized in Algorithm 1.

---

**Algorithm 1** Bidirectional Feature Fusion (BFF)

**Input:** LiDAR points  $\mathbf{P}_{pt}$ , image  $\mathbf{I}$ , camera parameters  $\mathbf{T}$   
**Output:** mm-aware PV features  $\mathbf{F}_{pv}$ , BEV features  $\mathbf{F}_{bev}$ ,  
“mm” denotes multi-modal.

```

 $\mathbf{F}_{pt}^{s1} = \text{PillarNet-S1}(\mathbf{P}_{pt})$ ,  $\mathbf{F}_{pv}^{s1} = \text{ResNet-S1}(\mathbf{I})$ 
     $\triangleright SI: \text{stage one.}$ 
 $\mathbf{P}_{pt2pv} = \{(u_i, v_i) | i \in P\} = \text{Project}(\mathbf{T}, \mathbf{P}_{pt})$ 
 $\mathbf{F}_{pt2pv} = \text{Scatter}(idx = \mathbf{P}_{pt2pv}, src = \mathbf{F}_{pt}^{s1})$ 
     $\triangleright \text{points} \rightarrow \text{pixels.}$ 
 $\mathbf{F}_{pv2pt} = \text{Grid.Sample}(src = \mathbf{F}_{pv}^{s1}, coords = \mathbf{P}_{pt2pv})$ 
     $\triangleright \text{pixels} \rightarrow \text{points.}$ 
 $\mathbf{F}_{pv} = \text{ResNet}(\text{Concat}(\mathbf{F}_{pv}^{s1}, \mathbf{F}_{pt2pv}))$ 
 $\mathbf{F}_{bev} = \text{PillarNet}(\text{Concat}(\mathbf{F}_{pt}^{s1}, \mathbf{F}_{pv2pt}))$ 
     $\triangleright \text{dual-view multi-modal feature extraction.}$ 

```

---

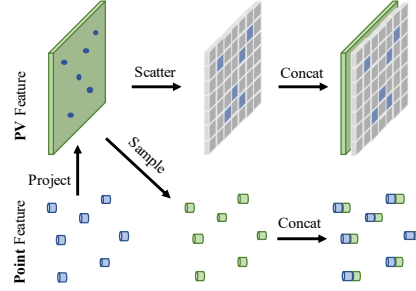


Figure 3: **Bidirectional Feature Fusion (BFF).** We represent the image feature in green and points in blue.

Concretely, we place points and images in their designated branches. After obtaining low-level features within each branch, we perform bidirectional feature fusion. By projecting 3D points  $\mathbf{P}_{pt} = \{(x_i, y_i, z_i) | i \in P\}$  onto the PV plane, we obtain their corresponding 2D coordinates  $\mathbf{P}_{pt2pv} = \{(u_i, v_i) | i \in P\}$ , where  $P$  is the cardinality of the point set. **1) For points-to-pixels** fusion, we utilize a Scatter operation to construct dense point feature grids  $\mathbf{F}_{pt2pv}$ , (depicted in the upper part of Figure 3, with blue cells denoting positions hit by the projected 3D points). **2) For pixels-to-points** fusion, we employ bilinear interpolation to sample features at 2D positions hit by the projection of 3D points, yielding  $\mathbf{F}_{pv2pt}$  (shown in the lower part of Figure 3). The resulting cross-modal features in PV and BEV are concatenated with their respective original modal features. The fused multi-modal features in each view, *i.e.*, PV and BEV, are then fed into subsequent modules in the corresponding branch, generating  $\mathbf{F}_{pv}$  and  $\mathbf{F}_{bev}$ , respectively. Notably,  $\mathbf{F}_{pv}$  and  $\mathbf{F}_{bev}$  encapsulate multi-modal information represented in distinct spaces.

### 3.2 UNIFIED QUERY GENERATOR

We introduce a unified query generator for end-to-end 3D lane detection. To this end, we first generate two distinct lane-aware query sets, termed dual-view queries, from the previously obtained multi-modal features,  $\mathbf{F}_{pv}$  and  $\mathbf{F}_{bev}$ . Then, we present a lane-centric clustering strategy to unify these dual-view queries into a cohesive set of queries.

**Dual-view Query Generation.** To effectively capture semantic and spatial features related to lanes, which are termed as “lane-aware” knowledge, we utilize an instance activation map (IAM) Cheng et al. (2022)-assisted method to generate lane-aware queries in PV and BEV spaces. Taking PV branch as an example, we produce a set of IAMs, denoted as  $\mathbf{A}_{pv}$ , via the following equation:

$$\mathbf{A}_{pv} = \sigma(\mathcal{F}(\text{Concat}(\mathbf{F}_{pv}, \mathbf{S}_{pv}))),$$

where  $\mathbf{A}_{pv} \in \mathbb{R}^{N \times H_{pv} \times W_{pv}}$ ,  $\mathbf{F}_{pv} \in \mathbb{R}^{C \times H_{pv} \times W_{pv}}$ ,  $N$  denotes query number,  $\sigma$  is the sigmoid function, Concat represents concatenation operation, and  $\mathbf{S}_{pv}$  comprises two-channel spatial localization features for each pixel Liu et al. (2018). The lane-aware query  $\mathbf{Q}_{pv}$  assisted by IAMs is generated via:

$$\mathbf{Q}_{pv} = \mathbf{A}_{pv} \otimes \mathbf{F}_{pv}^T,$$

where  $\mathbf{Q}_{pv} \in \mathbb{R}^{N \times C}$ ,  $\otimes$  denotes the matrix product. Similarly, lane-aware BEV query  $\mathbf{Q}_{bev} \in \mathbb{R}^{N \times C}$  is formed using:

$$\mathbf{Q}_{bev} = \sigma(\mathcal{F}([\mathbf{F}_{bev}, \mathbf{S}_{bev}])) \otimes \mathbf{F}_{bev}^T.$$

To force the query sets to learn lane-aware features, during training, we employ an auxiliary instance segmentation for each branch on top of the query set. Labels for the auxiliary segmentation are generated in pairs for these two branches, which are further assigned to predictions using mask-based bipartite matching Cheng et al. (2022), as illustrated in Figure 4 (a) and (b).

**Dual-view Query Clustering.** Given dual-view query sets  $\mathbf{Q}_{pv}$  and  $\mathbf{Q}_{bev}$ , we propose employing a *lane-centric* clustering technique to generate a unified query set for end-to-end lane detection. While kMax-DeepLab Yu et al. (2022) previously used k-means cross-attention to group pixels into distinct clusters, *i.e.*, instance masks, our approach focuses on unifying queries from different views. Queries from  $\mathbf{Q}_{pv}$  and  $\mathbf{Q}_{bev}$  targeting the same lane are merged within the same cluster. Specifically, we initiate lane cluster centers  $\mathbf{C} \in \mathbb{R}^{N \times C}$  with  $\mathbf{Q}_{pv}$ , and assign each query in  $\mathbf{Q}_{bev}$  to its nearest cluster center among  $\mathbf{C}$ . Notably, cluster centers can be chosen from either  $\mathbf{Q}_{pv}$  or  $\mathbf{Q}_{bev}$ . Empirically, we found that using  $\mathbf{Q}_{pv}$  produces better results. To achieve clustering, we perform attention between  $\mathbf{C}$  (query) and  $\mathbf{Q}_{bev}$  (key), while applying argmax along the cluster center (query) dimension Yu et al. (2022) as follows:

$$\mathbf{A} = \underset{N}{\text{argmax}}(\mathbf{C} \times \mathbf{Q}_{bev}^T), \quad \hat{\mathbf{C}} = \mathbf{A} \cdot \mathbf{Q}_{bev} + \mathbf{C},$$

where  $\hat{\mathbf{C}} \in \mathbb{R}^{N \times C}$  refers to updated centers unifying queries from dual views. In practise, we use gumbel-softmax Jang et al. (2016); Liang et al. (2023) to substitute argmax.

Considering the variation and slenderness of lanes, we employ a refined point query scheme Luo et al. (2023) to enhance lane detection. Instead of using a single query for each lane, multiple-point queries are employed for more precise capture Luo et al. (2023); Liao et al. (2022); Zhang et al. (2021a); Liu et al. (2023a). Consequently, in the first layer, we construct point-based queries  $\mathbf{Q} \in \mathbb{R}^{N \times M \times C}$  with  $\mathbf{Q} = \hat{\mathbf{C}} \oplus \mathbf{E}_{points}$ , where  $\oplus$  denotes broadcast sum,  $\mathbf{E}_{points} \in \mathbb{R}^{M \times C}$  is the learnable point embedding, and in the subsequent layer, we update  $\mathbf{Q}$  by  $\mathbf{Q} = \hat{\mathbf{C}} \oplus \mathbf{Q}$ .

**Supervision on Query Clustering.** Given the critical importance of deep supervision for the clustering Yu et al. (2022), we leverage the InfoNCE loss Oord et al. (2018); Radford et al. (2021), to supervise the query clustering in a lane-centric manner, as illustrated in Figure 4 (c) and formulated as Equation (1), where  $\tau$  is a temperature hyper-parameter Wu et al. (2018),  $q$  denotes one query,  $k^+$  indicates the positive sample *w.r.t.*  $q$ , and  $\mathcal{N}$  denotes the collection of all negative samples from the

different query set relative to the one containing  $q$ . Notably, queries assigned to the background do not incur penalties in the clustering learning process. With this supervision, queries from different views are grouped together when matched to the same ground truth lane. Consequently, lane-aware knowledge residing in two view spaces is synergized into the unified query.

$$\mathcal{L}_{\text{NCE}} = -\log \frac{\exp(\mathbf{q} \cdot \mathbf{k}^+ / \tau)}{\exp(\mathbf{q} \cdot \mathbf{k}^+ / \tau) + \sum_{\mathbf{k}^- \in \mathcal{N}} \exp(\mathbf{q} \cdot \mathbf{k}^- / \tau)}, \quad (1)$$

### 3.3 3D DUAL-VIEW DEFORMABLE ATTENTION

Apart from informative query generation, feature aggregation plays a crucial role in DV-3DLane. Instead of projecting points from densely sampled grids Chen et al. (2022) or their lifted pillars Li et al. (2022d) onto the PV plane for feature sampling, as shown in Figure 5 (a), we adopt sparse queries to sample features from different views. Moreover, our approach distinguishes itself from several existing sparse query methods, as depicted in Figure 5 (b) and (c). For instance, DeepInteraction Yang et al. (2022) (Figure 5 (b)) employs a sequential method to sample PV and BEV features, while FUTR3D Chen et al. (2023) (Figure 5 (c)) projects 3D points into different spaces, sampling features individually for each space.

In contrast, as outlined in Algorithm 2, we leverage the inherent properties of 3D space by predicting both 3D reference points and their 3D offsets Luo et al. (2022b) using queries, forming 3D deformed points. These 3D deformed points are then projected into each space, establishing a *consistent* feature sampling strategy across spaces, as depicted in Figure 5. Consequently, features corresponding to the same 3D points from different views are effectively sampled and integrated into the query.

---

**Algorithm 2** 3D DV Deformable Attention

---

**Input:** unified query set  $\mathbf{Q}$ , PV features  $\mathbf{F}_{pv}$ , BEV features  $\mathbf{F}_{bev}$ , camera parameters  $T$ .

**Output:** updated unified query  $\mathbf{Q}$ .

```

 $\mathbf{Ref}_{3d} = \text{MLP}_1(\mathbf{Q})$             $\triangleright 3D$  reference points.
 $\Delta\mathbf{Ref}_{3d} = \text{MLP}_2(\mathbf{Q})$ 
 $\mathbf{S}_{3d} = \{(x_i, y_i, z_i) | i \in N\} = \Delta\mathbf{Ref}_{3d} + \mathbf{Ref}_{3d}$             $\triangleright$  deformed 3D positions.
 $\mathbf{D}_{pv} = \text{DeformAttn}(\text{Project}_{pv}(\mathbf{S}_{3d}, T), \mathbf{F}_{pv})$             $\triangleright$  project 3D deformed points to PV.
 $\mathbf{D}_{bev} = \text{DeformAttn}(\text{Project}_{bev}(\mathbf{S}_{3d}), \mathbf{F}_{bev})$ 
 $\mathbf{Q} = \text{SE}(\mathbf{D}_{pv}, \mathbf{D}_{bev})$ 

```

---

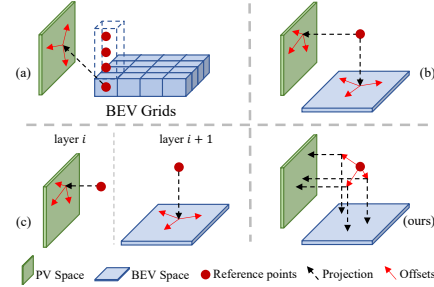


Figure 5: Illustration comparing 3D dual-view deformable attention with other approaches.

### 3.4 PREDICTION AND LOSS

**Auxiliary Tasks.** During training, we incorporate two auxiliary tasks: 1) 2D instance segmentation Luo et al. (2023); Cheng et al. (2022) loss  $\mathcal{L}_{seg}$  for both PV and BEV branches, aiding in extracting discriminative lane features in each view; 2) Depth estimation for the PV branch, which guides effective 3D structure-aware feature extraction of  $\mathbf{F}_{pv}$ . Depth labels are generated from LiDAR points, and the loss  $\mathcal{L}_{depth}$  is calculated following BEVDepth Li et al. (2022c).

**3D Lane Prediction and Loss.** As we adopt point-based queries  $\mathbf{Q} \in \mathbb{R}^{(N \times M) \times C}$ , each query naturally corresponds to a 3D point, and every group of  $M$  points constructs a complete 3D lane. Thus, we predict x, z, and visibility for each point query on the predefined y coordinates Chen et al. (2022); Luo et al. (2023) and a classification probability for each lane. Overall, the total loss is:

$$\begin{aligned} \mathcal{L}_{lane} &= w_x \mathcal{L}_x + w_z \mathcal{L}_z + w_v \mathcal{L}_v + w_c \mathcal{L}_c, \\ \mathcal{L}_{aux} &= w_{seg} \mathcal{L}_{seg} + w_{depth} \mathcal{L}_{depth}, \\ \mathcal{L}_{total} &= \mathcal{L}_{lane} + \mathcal{L}_{aux}. \end{aligned}$$

where  $w_*$  denotes different loss weights. We adopt the L1 loss  $\mathcal{L}_x$  and  $\mathcal{L}_z$  to learn the x, z positions, focal loss Lin et al. (2017)  $\mathcal{L}_c$  to learn the lane category, and BCELoss  $\mathcal{L}_v$  to learn visibility.

## 4 EXPERIMENTS

### 4.1 DATASETS

We evaluate our method on OpenLane Chen et al. (2022), the *sole* public 3D lane dataset featuring multi-modal sources, OpenLane is a large-scale dataset built on Waymo Open Dataset Sun et al. (2020), comprising 200K frames and 880K lanes across six driving scenarios and 14 lane categories. The LiDAR data, collected using 64-beam LiDARs, is sampled at 10Hz. This extensive dataset provides a solid foundation for evaluating 3D lane algorithms comprehensively.

### 4.2 METRICS

We adopt the evaluation metrics established by OpenLane Chen et al. (2022), framing 3D lane detection evaluation as a matching problem based on the edit distance between predictions and ground truth. Successful matching results in computed metrics, including F-Score, category accuracy, and error in X/Z-axes. A successful match for each predicted 3D lane is defined when at least 75% of its points have a distance to the ground truth below the predefined threshold  $D_{thre}$ .

### 4.3 IMPLEMENTATION DETAILS

**Models.** In the base version of DV-3DLane, we employ ResNet34 He et al. (2016) and PillarNet34 Shi et al. (2022) as the backbones for our camera and LiDAR branches, respectively. For the lite version, we utilize ResNet18 and PillarNet18, while the lite version employs a single decoder layer. Following LATR Luo et al. (2023), we set the number of lane queries to 40, and we employ deformable attention with 4 heads, 8 sample points, and 256 embedding dimensions.

**Training.** We use the Adam optimizer Kingma & Ba (2014) with a weight decay of 0.01. The learning rate is set to 2e-4, and our models undergo training for 24 epochs with a batch size of 32. We employ the cosine annealing scheduler Loshchilov & Hutter (2016) with  $T_{max} = 8$ . Our input images are of resolution 720×960, and we adopt a voxel size of (0.2m, 0.4m) for the X and Y axes.

### 4.4 MAIN RESULTS

It's important to note that the existing metrics use a rather *lenient* distance threshold of  $D_{thre}=1.5\text{m}$ . However, this value, although commonly used for assessment purposes, may be considered overly permissive in the context of ensuring safety in AD. Following M<sup>2</sup>-3DLaneNet Luo et al. (2022a), we extend our evaluation to include a *more stringent* threshold,  $D_{thre}=0.5\text{m}$ . Further, we illustrate the relationship between the F1 score performance and different distance thresholds for various models, as shown in Figure 6. Notably, our method consistently achieves superior results, even when evaluated under a *much more stringent* criterion of  $D_{thre}=0.1\text{m}$ . In contrast, other approaches experience a noticeable decline in performance as the distance threshold decreases. These findings confirm the robustness of our method across varying distance thresholds, particularly highlighting its advantage in precise localization.

We present the main results in Table 1, obtained from experiments conducted on the OpenLane-1K dataset. The evaluation uses both  $D_{thre}=1.5\text{m}$  and  $D_{thre}=0.5\text{m}$  criteria, allowing for a comprehensive and insightful comparison. It is evident that DV-3DLane consistently outperforms previous state-of-the-art (SoTA) methods across all metrics. Notably, when applying a more strict 0.5m threshold, DV-3DLane demonstrates a substantial **11.2%** improvement in the F1 score. Notably, our method excels in localization accuracy, leading to significant performance improvements. Specifically, our method achieves remarkable reductions in localization errors: 52%/50% for X near/far

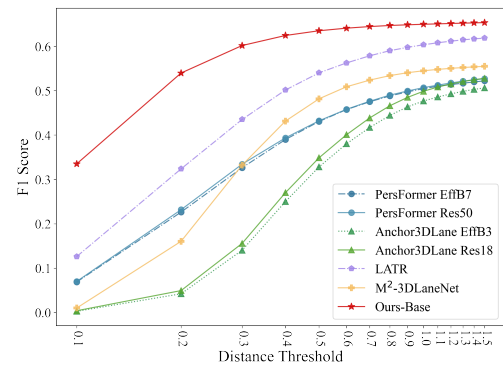


Figure 6: **F1 score vs. Distance Threshold.** Our method consistently achieves superior results under more stringent criteria.

The base version features two decoder layers, while the lite version employs a single decoder layer. Following LATR Luo et al. (2023), we set the number of lane queries to 40, and we employ deformable attention with 4 heads, 8 sample points, and 256 embedding dimensions.

Table 1: Comprehensive 3D Lane evaluation comparison on OpenLane with variable metrics.  $\dagger$  denotes the results obtained using their provided models. “Image-Branch” and “LiDAR-Branch” refer to our image and LiDAR branches, respectively. “LATR + LiDAR” denotes the model that combines the SOTA method LATR with LiDAR input, projecting all points into the image space and using them as additional features in the network.

Dist.	Methods	Backbone	Modality	F1↑	Acc.↑	X error (m)↓		Z error (m)↓	
						near	far	near	far
1.5 m	3DLaneNet Garnett et al. (2019)	VGG-16	C	44.1	-	0.593	0.494	0.140	0.195
	GenLaneNet Guo et al. (2020)	ERFNet	C	32.3	-	0.591	0.684	0.411	0.521
	PersFormer Chen et al. (2022)	EffNet-B7	C	50.5	89.5	0.319	0.325	0.112	0.141
	Anchor3DLane Huang et al. (2023) $\dagger$	EffNet-B3	C	52.8	89.6	0.408	0.349	0.186	0.143
	M <sup>2</sup> -3DLaneNet Luo et al. (2022a)	EffNet-B7	C+L	55.5	88.2	0.283	0.256	0.078	0.106
	Anchor3DLane Huang et al. (2023) $\dagger$	ResNet-18	C	50.7	89.3	0.422	0.349	0.188	0.146
	PersFormer Chen et al. (2022)	ResNet-50	C	52.7	88.4	0.307	0.319	0.083	0.117
	LATR Luo et al. (2023)	ResNet-50	C	61.9	92.0	0.219	0.259	0.075	0.104
	DV-3DLane-Tiny (Ours)	ResNet-18	C+L	63.4	91.6	0.137	0.159	0.034	0.063
	DV-3DLane-Base (Ours)	ResNet-34	C+L	65.4	92.4	0.118	0.131	0.032	0.053
	DV-3DLane-Large (Ours)	ResNet-50	C+L	<b>66.8</b>	<b>93.3</b>	<b>0.115</b>	<b>0.134</b>	<b>0.029</b>	<b>0.049</b>
<i>Improvement</i>		-	-	<b>14.9</b>	<b>↑1.3</b>	<b>↓0.104</b>	<b>↓0.122</b>	<b>↓0.046</b>	<b>↓0.055</b>
0.5 m	PersFormer Chen et al. (2022)	EffNet-B7	C	36.5	87.8	0.343	0.263	0.161	0.115
	Anchor3DLane Huang et al. (2023) $\dagger$	EffNet-B3	C	34.9	88.5	0.344	0.264	0.181	0.134
	M <sup>2</sup> -3DLaneNet Luo et al. (2022a)	EffNet-B7	C+L	48.2	88.1	0.217	0.203	0.076	0.103
	Anchor3DLane Huang et al. (2023) $\dagger$	ResNet-18	C	32.8	87.9	0.350	0.266	0.183	0.137
	PersFormer Chen et al. (2022)	ResNet-50	C	43.2	87.8	0.229	0.245	0.078	0.106
	LATR Luo et al. (2023)	ResNet-50	C	54.0	91.7	0.171	0.201	0.072	0.099
	LATR + LiDAR	ResNet-50	C+L	57.4	92.1	0.167	0.185	0.071	0.088
	Image-Branch (Ours)	ResNet-34	C	52.9	90.3	0.173	0.212	0.069	0.098
	LiDAR-Branch (Ours)	PillarN-34	L	54.1	84.4	0.282	0.191	0.096	0.124
	DV-3DLane-Tiny (Ours)	ResNet-18	C+L	60.9	91.8	0.097	0.124	0.033	0.062
	DV-3DLane-Base (Ours)	ResNet-34	C+L	63.5	92.4	0.090	0.102	0.031	0.053
	DV-3DLane-Large (Ours)	ResNet-50	C+L	<b>65.2</b>	<b>93.4</b>	<b>0.082</b>	<b>0.101</b>	<b>0.028</b>	<b>0.048</b>
<i>Improvement</i>		-	-	<b>↑11.2</b>	<b>↑1.7</b>	<b>↓0.089</b>	<b>↓0.100</b>	<b>↓0.044</b>	<b>↓0.051</b>

and 61%/52% for Z near/far. Due to space limitations, results in various scenarios and studies about robustness concerning calibration noise are included in the Appendix.

**Effect of Multiple Modalities.** To explore the impact of individual modalities, we conduct experiments using single modalities, as outlined in the “Image-Branch” and “LiDAR-Branch” rows of Table 1. The results illustrate that DV-3DLane significantly enhances performance compared to using images alone or relying solely on LiDAR data. Notably, our method significantly surpasses configurations that simply equip LATR with LiDAR input across all metrics, underscoring the substantial improvements achieved by DV-3DLane in leveraging information from both modalities. Moreover, to evaluate the effect of **dual-view**, we conduct experiments using single-modality input but transforming features extracted from the backbone into another view, yielding single-modal dual-view features. Then, our dual-view decoder is applied, and the results are detailed in the Appendix. Additionally, we conduct experiments using our “Image-Branch” on the Apollo Guo et al. (2020) dataset, which exclusively contains image data. The results are provided in the Appendix.

**Qualitative Results.** We present a qualitative comparison between DV-3DLane and LATR Luo et al. (2023) in Figure 7, demonstrating that our method achieves more robust and accurate predictions across various scenarios. More visualization results are included in the Appendix.

#### 4.5 ABLATION STUDIES

We conduct all ablation studies on OpenLane-300 following established practices Chen et al. (2022); Luo et al. (2023); Huang et al. (2023), while adopting a **0.5m** threshold  $D_{thre}$  for evaluation.

**Effect of Bidirectional Feature Fusion.** The corresponding experiments are included in the Appendix due to space limitations. We kindly direct the readers to refer to the Appendix for details. The results confirm the effectiveness of the proposed bidirectional feature fusion approach.

**Effect of Unified Query.** We study the effect of our unified query generation strategy in Table 2, where “Random” means random initialization using `nn.Embedding`, “ $Q_{pv}$ ” denotes using only PV queries, and “ $Q_{bev}$ ” refers to using only BEV queries. Replacing our unified queries with randomly initialized ones Carion et al. (2020); Zhu et al. (2020); Li et al. (2022d) results in a decrease of 1.0 in the F1 score compared to our approach. Interestingly, employing a single space instance-

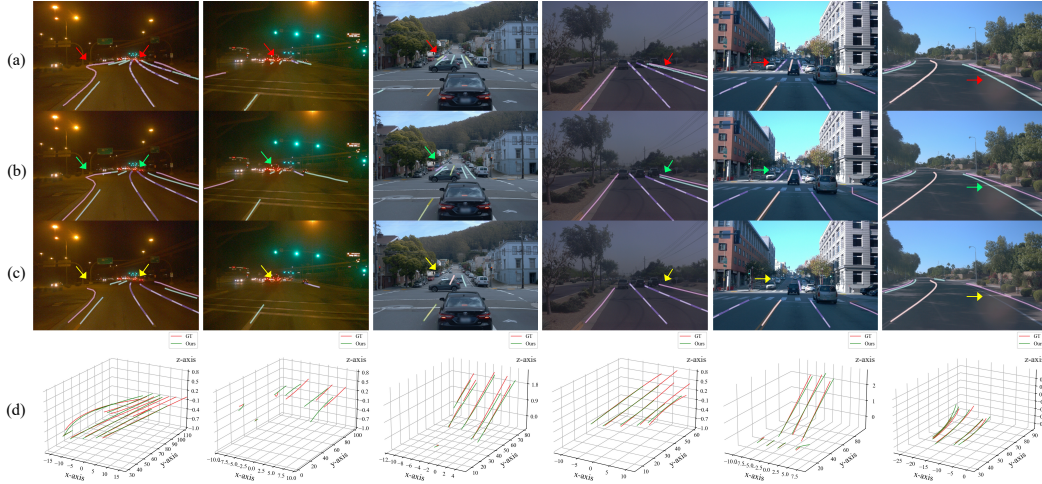


**Figure 7: Qualitative Results.** We present the projection of 3D lanes from **ground truth**, predictions of **DV-3DLane** and the SOTA method **LART** Luo et al. (2023) in rows (a), (b), (c), respectively. Row (d) depicts the comparison between **ground truth** (red) and **ours** (green) in 3D space. We highlight the differences with colored arrows. Best viewed in color and zoom in for details.

aware query yields even lower F1 scores of 69.6%/69.1% for PV/BEV, respectively, than random initialization. This underscores the inadequacy of a single-space lane-aware query in capturing complex 3D lane features comprehensively existing in both PV and BEV spaces. However, our dual-view strategy, generating lane-aware queries *w.r.t.* both views, improves overall performance to 70.7, achieving the best result. This demonstrates that our method effectively integrates the strengths of features from two spaces, forming a cohesive query set.

**Effect of 3D Dual-view Deformable Attention.** To evaluate the efficacy of our proposed Dual-view Deformable Attention, we conduct ablation studies in Table 3, where “PV space” and “BEV space” mean using single space in the decoder. “DeepInteration” Yang et al. (2022) denotes sequential fusion of features from different spaces, and “FUTR3D” Chen et al. (2023) refer to a modality-agnostic approach where sampling locations differ across views. We compare DV-3DLane against alternative approaches, including the single-view fused method, as well as methods proposed in DeepInteration and FUTR3D, as described in Section 3.3. The results underscore the significance of our approach. In detail, sampling only PV space features leads to a notable drop ( $70.7 \rightarrow 63.6$ ) in performance, showing the importance of BEV space due to its advantages in localization. Besides, our method outperforms the sequential approach of DeepInteration with a substantial 2.0 gain in F1 score. Furthermore, compared to the modality-agnostic approach proposed in FUTR3D, our method achieves a 0.5 improvement, emphasizing the importance of consistent sampling locations in deformable attention across different spaces.

Table 2: Effect of unified query.

Methods	F1	X error (m)		Z error (m)	
		near	far	near	far
Random	69.7	0.123	0.151	0.059	0.081
$Q_{pv}$	69.6	0.124	0.155	0.059	0.079
$Q_{bev}$	69.1	0.122	0.145	0.058	0.077
Ours	70.7	0.123	0.146	0.058	0.078

Table 3: Effect of 3D dual-view deformable attention.

Methods	F1	X error (m)		Z error (m)	
		near	far	near	far
PV space	63.6	0.150	0.202	0.060	0.081
BEV space	68.5	0.127	0.151	0.064	0.087
DeepInteration	68.7	0.126	0.157	0.059	0.081
FUTR3D	70.2	0.118	0.145	0.057	0.077
Ours	70.7	0.123	0.146	0.058	0.078

## 5 CONCLUSION

In this work, we introduce DV-3DLane, a novel end-to-end multi-modal 3D lane detection framework that leverages the strengths of both PV and BEV spaces. To this end, we propose three novel modules that effectively utilize dual-view representation on different levels, consistently enhancing performance. Extensive experiments substantiate the outstanding advancements achieved by DV-3DLane, establishing a new state of the art on OpenLane.

## ACKNOWLEDGMENTS

This work was supported by NSFC with Grant No. 62293482, by the Basic Research Project No. HZQB-KCXYZ-2021067 of Hetao Shenzhen HK S&T Cooperation Zone, by Shenzhen General Program No. JCYJ20220530143600001, by Shenzhen-Hong Kong Joint Funding No. SGDX2021123112401002, by the National Key R&D Program of China with grant No. 2018YFB1800800, by the Shenzhen Outstanding Talents Training Fund 202002, by Guangdong Research Project No. 2017ZT07X152 and No. 2019CX01X104, by the Guangdong Provincial Key Laboratory of Future Networks of Intelligence (Grant No. 2022B1212010001), by the Guangdong Provincial Key Laboratory of Big Data Computing, The Chinese University of Hong Kong, Shenzhen, by the NSFC 61931024&12326610, by the Shenzhen Key Laboratory of Big Data and Artificial Intelligence (Grant No. ZDSYS201707251409055), and the Key Area R&D Program of Guangdong Province with grant No. 2018B03033800, by Tencent&Huawei Open Fund.

## REFERENCES

- Jianyong Ai, Wenbo Ding, Jiuhsia Zhao, and Jiachen Zhong. Ws-3d-lane: Weakly supervised 3d lane detection with 2d lane labels. In *2023 IEEE International Conference on Robotics and Automation (ICRA)*, pp. 5595–5601. IEEE, 2023.
- Min Bai, Gellert Mattus, Namdar Homayounfar, Shenlong Wang, Shrinidhi Kowshika Lakshmanth, and Raquel Urtasun. Deep multi-sensor lane detection. In *2018 IEEE/RSJ International Conference on Intelligent Robots and Systems (IROS)*, pp. 3102–3109. IEEE, 2018.
- Xuyang Bai, Zeyu Hu, Xinge Zhu, Qingqiu Huang, Yilun Chen, Hongbo Fu, and Chiew-Lan Tai. Transfusion: Robust lidar-camera fusion for 3d object detection with transformers. In *Proceedings of the IEEE/CVF conference on computer vision and pattern recognition*, pp. 1090–1099, 2022a.
- Yifeng Bai, Zhirong Chen, Zhangjie Fu, Lang Peng, Pengpeng Liang, and Erkang Cheng. Curveformer: 3d lane detection by curve propagation with curve queries and attention. *arXiv preprint arXiv:2209.07989*, 2022b.
- Nicolas Carion, Francisco Massa, Gabriel Synnaeve, Nicolas Usunier, Alexander Kirillov, and Sergey Zagoruyko. End-to-end object detection with transformers. In *Computer Vision–ECCV 2020: 16th European Conference, Glasgow, UK, August 23–28, 2020, Proceedings, Part I 16*, pp. 213–229. Springer, 2020.
- Li Chen, Chonghao Sima, Yang Li, Zehan Zheng, Jiajie Xu, Xiangwei Geng, Hongyang Li, Conghui He, Jianping Shi, Yu Qiao, and Junchi Yan. Persformer: 3d lane detection via perspective transformer and the openlane benchmark. In *European Conference on Computer Vision (ECCV)*, 2022.
- Xuanyao Chen, Tianyuan Zhang, Yue Wang, Yilun Wang, and Hang Zhao. Futr3d: A unified sensor fusion framework for 3d detection. In *Proceedings of the IEEE/CVF Conference on Computer Vision and Pattern Recognition*, pp. 172–181, 2023.
- Tianheng Cheng, Xinggang Wang, Shaoyu Chen, Wenqiang Zhang, Qian Zhang, Chang Huang, Zhaoxiang Zhang, and Wenyu Liu. Sparse instance activation for real-time instance segmentation. In *Proceedings of the IEEE/CVF Conference on Computer Vision and Pattern Recognition*, pp. 4433–4442, 2022.
- Netalee Efrat, Max Bluvstein, Shaul Oron, Dan Levi, Noa Garnett, and Bat El Shlomo. 3d-lanenet+: Anchor free lane detection using a semi-local representation. *arXiv preprint arXiv:2011.01535*, 2020.
- Zhengyang Feng, Shaohua Guo, Xin Tan, Ke Xu, Min Wang, and Lizhuang Ma. Rethinking efficient lane detection via curve modeling. In *Proceedings of the IEEE/CVF Conference on Computer Vision and Pattern Recognition*, pp. 17062–17070, 2022.
- Noa Garnett, Rafi Cohen, Tomer Pe'er, Roee Lahav, and Dan Levi. 3d-lanenet: end-to-end 3d multiple lane detection. In *Proceedings of the IEEE/CVF International Conference on Computer Vision*, pp. 2921–2930, 2019.

- Yuliang Guo, Guang Chen, Peitao Zhao, Weide Zhang, Jinghao Miao, Jingao Wang, and Tae Eun Choe. Gen-lanenet: A generalized and scalable approach for 3d lane detection. In *European Conference on Computer Vision*, pp. 666–681. Springer, 2020.
- Kaiming He, Xiangyu Zhang, Shaoqing Ren, and Jian Sun. Deep residual learning for image recognition. In *Proceedings of the IEEE conference on computer vision and pattern recognition*, pp. 770–778, 2016.
- Yuenan Hou, Zheng Ma, Chunxiao Liu, and Chen Change Loy. Learning lightweight lane detection cnns by self attention distillation. In *Proceedings of the IEEE/CVF international conference on computer vision*, pp. 1013–1021, 2019.
- Shaofei Huang, Zhenwei Shen, Zehao Huang, Zi-han Ding, Jiao Dai, Jizhong Han, Naiyan Wang, and Si Liu. Anchor3dlane: Learning to regress 3d anchors for monocular 3d lane detection. In *Proceedings of the IEEE/CVF Conference on Computer Vision and Pattern Recognition*, pp. 17451–17460, 2023.
- Eric Jang, Shixiang Gu, and Ben Poole. Categorical reparameterization with gumbel-softmax. *arXiv preprint arXiv:1611.01144*, 2016.
- Dongkwon Jin, Wonhui Park, Seong-Gyun Jeong, Heeyeon Kwon, and Chang-Su Kim. Eigenlanes: Data-driven lane descriptors for structurally diverse lanes. In *Proceedings of the IEEE/CVF Conference on Computer Vision and Pattern Recognition*, pp. 17163–17171, 2022.
- Diederik P Kingma and Jimmy Ba. Adam: A method for stochastic optimization. *arXiv preprint arXiv:1412.6980*, 2014.
- Yeongmin Ko, Younkwon Lee, Shoaib Azam, Farzeen Munir, Moongu Jeon, and Witold Pedrycz. Key points estimation and point instance segmentation approach for lane detection. *IEEE Transactions on Intelligent Transportation Systems*, 23(7):8949–8958, 2021.
- Alex H Lang, Sourabh Vora, Holger Caesar, Lubing Zhou, Jiong Yang, and Oscar Beijbom. Point-pillars: Fast encoders for object detection from point clouds. In *Proceedings of the IEEE/CVF conference on computer vision and pattern recognition*, pp. 12697–12705, 2019.
- Seokju Lee, Junsik Kim, Jae Shin Yoon, Seunghak Shin, Oleksandr Bailo, Namil Kim, Tae-Hee Lee, Hyun Seok Hong, Seung-Hoon Han, and In So Kweon. Vpgnet: Vanishing point guided network for lane and road marking detection and recognition. In *Proceedings of the IEEE international conference on computer vision*, pp. 1947–1955, 2017.
- Chenguang Li, Jia Shi, Ya Wang, and Guangliang Cheng. Reconstruct from top view: A 3d lane detection approach based on geometry structure prior. In *Proceedings of the IEEE/CVF Conference on Computer Vision and Pattern Recognition*, pp. 4370–4379, 2022a.
- Xiang Li, Jun Li, Xiaolin Hu, and Jian Yang. Line-cnn: End-to-end traffic line detection with line proposal unit. *IEEE Transactions on Intelligent Transportation Systems*, 21(1):248–258, 2019.
- Yingwei Li, Adams Wei Yu, Tianjian Meng, Ben Caine, Jiquan Ngiam, Daiyi Peng, Junyang Shen, Yifeng Lu, Denny Zhou, Quoc V Le, et al. Deepfusion: Lidar-camera deep fusion for multi-modal 3d object detection. In *Proceedings of the IEEE/CVF Conference on Computer Vision and Pattern Recognition*, pp. 17182–17191, 2022b.
- Yinhao Li, Zheng Ge, Guanyi Yu, Jinrong Yang, Zengran Wang, Yukang Shi, Jianjian Sun, and Zeming Li. Bevdepth: Acquisition of reliable depth for multi-view 3d object detection. *arXiv preprint arXiv:2206.10092*, 2022c.
- Zhiqi Li, Wenhui Wang, Hongyang Li, Enze Xie, Chonghao Sima, Tong Lu, Yu Qiao, and Jifeng Dai. Bevformer: Learning bird’s-eye-view representation from multi-camera images via spatiotemporal transformers. In *Computer Vision–ECCV 2022: 17th European Conference, Tel Aviv, Israel, October 23–27, 2022, Proceedings, Part IX*, pp. 1–18. Springer, 2022d.
- James Liang, Tianfei Zhou, Dongfang Liu, and Wenguan Wang. Clustseg: Clustering for universal segmentation. *arXiv preprint arXiv:2305.02187*, 2023.

- Ming Liang, Bin Yang, Yun Chen, Rui Hu, and Raquel Urtasun. Multi-task multi-sensor fusion for 3d object detection. In *Proceedings of the IEEE/CVF Conference on Computer Vision and Pattern Recognition*, pp. 7345–7353, 2019.
- Tingting Liang, Hongwei Xie, Kaicheng Yu, Zhongyu Xia, Zhiwei Lin, Yongtao Wang, Tao Tang, Bing Wang, and Zhi Tang. Bevfusion: A simple and robust lidar-camera fusion framework. *Advances in Neural Information Processing Systems*, 35:10421–10434, 2022.
- Bencheng Liao, Shaoyu Chen, Xinggang Wang, Tianheng Cheng, Qian Zhang, Wenyu Liu, and Chang Huang. Maptr: Structured modeling and learning for online vectorized hd map construction. *arXiv preprint arXiv:2208.14437*, 2022.
- Tsung-Yi Lin, Priya Goyal, Ross Girshick, Kaiming He, and Piotr Dollár. Focal loss for dense object detection. In *Proceedings of the IEEE international conference on computer vision*, pp. 2980–2988, 2017.
- Huan Liu, Qiang Chen, Zichang Tan, Jiang-Jiang Liu, Jian Wang, Xiangbo Su, Xiaolong Li, Kun Yao, Junyu Han, Errui Ding, et al. Group pose: A simple baseline for end-to-end multi-person pose estimation. *arXiv preprint arXiv:2308.07313*, 2023a.
- Rosanne Liu, Joel Lehman, Piero Molino, Felipe Petroski Such, Eric Frank, Alex Sergeev, and Jason Yosinski. An intriguing failing of convolutional neural networks and the coordconv solution. *Advances in neural information processing systems*, 31, 2018.
- Ruijin Liu, Zejian Yuan, Tie Liu, and Zhiliang Xiong. End-to-end lane shape prediction with transformers. In *Proceedings of the IEEE/CVF winter conference on applications of computer vision*, pp. 3694–3702, 2021.
- Ruijin Liu, Dapeng Chen, Tie Liu, Zhiliang Xiong, and Zejian Yuan. Learning to predict 3d lane shape and camera pose from a single image via geometry constraints. In *Proceedings of the AAAI Conference on Artificial Intelligence*, volume 36, pp. 1765–1772, 2022.
- Zhijian Liu, Haotian Tang, Alexander Amini, Xinyu Yang, Huizi Mao, Daniela L Rus, and Song Han. Bevfusion: Multi-task multi-sensor fusion with unified bird’s-eye view representation. In *2023 IEEE International Conference on Robotics and Automation (ICRA)*, pp. 2774–2781. IEEE, 2023b.
- Ilya Loshchilov and Frank Hutter. Sgdr: Stochastic gradient descent with warm restarts. *arXiv preprint arXiv:1608.03983*, 2016.
- Yueru Luo, Xu Yan, Chaoda Zheng, Chao Zheng, Shuqi Mei, Tang Kun, Shuguang Cui, and Zhen Li. M<sup>^</sup> 2-3dlanenet: Multi-modal 3d lane detection. *arXiv preprint arXiv:2209.05996*, 2022a.
- Yueru Luo, Chaoda Zheng, Xu Yan, Tang Kun, Chao Zheng, Shuguang Cui, and Zhen Li. Latr: 3d lane detection from monocular images with transformer, 2023.
- Zhipeng Luo, Changqing Zhou, Gongjie Zhang, and Shijian Lu. Detr4d: Direct multi-view 3d object detection with sparse attention. *arXiv preprint arXiv:2212.07849*, 2022b.
- Zhipeng Luo, Changqing Zhou, Liang Pan, Gongjie Zhang, Tianrui Liu, Yueru Luo, Haiyu Zhao, Ziwei Liu, and Shijian Lu. Exploring point-bev fusion for 3d point cloud object tracking with transformer. *IEEE transactions on pattern analysis and machine intelligence*, 2024.
- Yuxin Ma, Tai Wang, Xuyang Bai, Huitong Yang, Yuenan Hou, Yaming Wang, Yu Qiao, Ruigang Yang, Dinesh Manocha, and Xinge Zhu. Vision-centric bev perception: A survey. *arXiv preprint arXiv:2208.02797*, 2022.
- Hanspeter A Mallot, Heinrich H Bülthoff, JJ Little, and Stefan Bohrer. Inverse perspective mapping simplifies optical flow computation and obstacle detection. *Biological cybernetics*, 64(3):177–185, 1991.
- Sergiu Nedevschi, Rolf Schmidt, Thorsten Graf, Radu Danescu, Dan Frentiu, Tiberiu Marita, Florin Oniga, and Ciprian Pocol. 3d lane detection system based on stereovision. In *Proceedings. The 7th International IEEE Conference on Intelligent Transportation Systems (IEEE Cat. No. 04TH8749)*, pp. 161–166. IEEE, 2004.

- Davy Neven, Bert De Brabandere, Stamatios Georgoulis, Marc Proesmans, and Luc Van Gool. Towards end-to-end lane detection: an instance segmentation approach. In *2018 IEEE intelligent vehicles symposium (IV)*, pp. 286–291. IEEE, 2018.
- Aaron van den Oord, Yazhe Li, and Oriol Vinyals. Representation learning with contrastive predictive coding. *arXiv preprint arXiv:1807.03748*, 2018.
- X Pan, J Shi, P Luo, X Wang, and X Tang. Spatial as deep: spatial cnn for traffic scene understanding. 2017. *Pan X Shi J Luo P Spatial As Deep: Spatial CNN for Traffic Scene Understanding*, 10, 2017.
- Jonah Philion and Sanja Fidler. Lift, splat, shoot: Encoding images from arbitrary camera rigs by implicitly unprojecting to 3d. In *Computer Vision–ECCV 2020: 16th European Conference, Glasgow, UK, August 23–28, 2020, Proceedings, Part XIV 16*, pp. 194–210. Springer, 2020.
- Zhan Qu, Huan Jin, Yang Zhou, Zhen Yang, and Wei Zhang. Focus on local: Detecting lane marker from bottom up via key point. In *Proceedings of the IEEE/CVF Conference on Computer Vision and Pattern Recognition*, pp. 14122–14130, 2021.
- Alec Radford, Jong Wook Kim, Chris Hallacy, Aditya Ramesh, Gabriel Goh, Sandhini Agarwal, Girish Sastry, Amanda Askell, Pamela Mishkin, Jack Clark, Gretchen Krueger, and Ilya Sutskever. Learning transferable visual models from natural language supervision, 2021.
- Shaoqing Ren, Kaiming He, Ross Girshick, and Jian Sun. Faster r-cnn: Towards real-time object detection with region proposal networks. *Advances in neural information processing systems*, 28, 2015.
- Guangsheng Shi, Ruifeng Li, and Chao Ma. Pillarnet: Real-time and high-performance pillar-based 3d object detection. In *European Conference on Computer Vision*, pp. 35–52. Springer, 2022.
- Vishwanath A Sindagi, Yin Zhou, and Oncel Tuzel. Mvx-net: Multimodal voxelnet for 3d object detection. In *2019 International Conference on Robotics and Automation (ICRA)*, pp. 7276–7282. IEEE, 2019.
- Pei Sun, Henrik Kretzschmar, Xerxes Dotiwalla, Aurelien Chouard, Vijaysai Patnaik, Paul Tsui, James Guo, Yin Zhou, Yuning Chai, Benjamin Caine, et al. Scalability in perception for autonomous driving: Waymo open dataset. In *Proceedings of the IEEE/CVF conference on computer vision and pattern recognition*, pp. 2446–2454, 2020.
- Lucas Tabelini, Rodrigo Berriel, Thiago M Paixao, Claudine Badue, Alberto F De Souza, and Thiago Oliveira-Santos. Keep your eyes on the lane: Real-time attention-guided lane detection. In *Proceedings of the IEEE/CVF conference on computer vision and pattern recognition*, pp. 294–302, 2021a.
- Lucas Tabelini, Rodrigo Berriel, Thiago M Paixao, Claudine Badue, Alberto F De Souza, and Thiago Oliveira-Santos. Polylanenet: Lane estimation via deep polynomial regression. In *2020 25th International Conference on Pattern Recognition (ICPR)*, pp. 6150–6156. IEEE, 2021b.
- Wouter Van Gansbeke, Bert De Brabandere, Davy Neven, Marc Proesmans, and Luc Van Gool. End-to-end lane detection through differentiable least-squares fitting. In *Proceedings of the IEEE/CVF International Conference on Computer Vision Workshops*, pp. 0–0, 2019.
- Chunwei Wang, Chao Ma, Ming Zhu, and Xiaokang Yang. Pointaugmenting: Cross-modal augmentation for 3d object detection. In *Proceedings of the IEEE/CVF Conference on Computer Vision and Pattern Recognition*, pp. 11794–11803, 2021.
- Jinsheng Wang, Yinchao Ma, Shaofei Huang, Tianrui Hui, Fei Wang, Chen Qian, and Tianzhu Zhang. A keypoint-based global association network for lane detection. In *Proceedings of the IEEE/CVF Conference on Computer Vision and Pattern Recognition*, pp. 1392–1401, 2022.
- Ruihao Wang, Jian Qin, Kaiying Li, Yaochen Li, Dong Cao, and Jintao Xu. Bev-lanedet: An efficient 3d lane detection based on virtual camera via key-points. In *Proceedings of the IEEE/CVF Conference on Computer Vision and Pattern Recognition*, pp. 1002–1011, 2023.

- Ze Wang, Weiqiang Ren, and Qiang Qiu. Lanenet: Real-time lane detection networks for autonomous driving. *arXiv preprint arXiv:1807.01726*, 2018.
- Zhirong Wu, Yuanjun Xiong, Stella X Yu, and Dahua Lin. Unsupervised feature learning via non-parametric instance discrimination. In *Proceedings of the IEEE conference on computer vision and pattern recognition*, pp. 3733–3742, 2018.
- Hang Xu, Shaoju Wang, Xinyue Cai, Wei Zhang, Xiaodan Liang, and Zhenguo Li. Curvelane-nas: Unifying lane-sensitive architecture search and adaptive point blending. In *Computer Vision-ECCV 2020: 16th European Conference, Glasgow, UK, August 23–28, 2020, Proceedings, Part XV 16*, pp. 689–704. Springer, 2020.
- Shenghua Xu, Xinyue Cai, Bin Zhao, Li Zhang, Hang Xu, Yanwei Fu, and Xiangyang Xue. Rclane: Relay chain prediction for lane detection. In *European Conference on Computer Vision*, pp. 461–477. Springer, 2022.
- Fan Yan, Ming Nie, Xinyue Cai, Jianhua Han, Hang Xu, Zhen Yang, Chaoqiang Ye, Yanwei Fu, Michael Bi Mi, and Li Zhang. Once-3dlanes: Building monocular 3d lane detection. In *Proceedings of the IEEE/CVF Conference on Computer Vision and Pattern Recognition*, pp. 17143–17152, 2022.
- Zeyu Yang, Jiaqi Chen, Zhenwei Miao, Wei Li, Xiatian Zhu, and Li Zhang. Deepinteraction: 3d object detection via modality interaction. *Advances in Neural Information Processing Systems*, 35:1992–2005, 2022.
- Chengtang Yao, Lidong Yu, Yuwei Wu, and Yunde Jia. Sparse point guided 3d lane detection. In *Proceedings of the IEEE/CVF International Conference on Computer Vision*, pp. 8363–8372, 2023.
- Ruochen Yin, Yong Cheng, Huapeng Wu, Yuntao Song, Biao Yu, and Runxin Niu. Fusionlane: Multi-sensor fusion for lane marking semantic segmentation using deep neural networks. *IEEE Transactions on Intelligent Transportation Systems*, 23(2):1543–1553, 2020.
- Tianwei Yin, Xingyi Zhou, and Philipp Krahenbuhl. Center-based 3d object detection and tracking. In *Proceedings of the IEEE/CVF conference on computer vision and pattern recognition*, pp. 11784–11793, 2021a.
- Tianwei Yin, Xingyi Zhou, and Philipp Krähenbühl. Multimodal virtual point 3d detection. *Advances in Neural Information Processing Systems*, 34:16494–16507, 2021b.
- Jin Hyeok Yoo, Yecheol Kim, Jisong Kim, and Jun Won Choi. 3d-cvf: Generating joint camera and lidar features using cross-view spatial feature fusion for 3d object detection. In *Computer Vision-ECCV 2020: 16th European Conference, Glasgow, UK, August 23–28, 2020, Proceedings, Part XXVII 16*, pp. 720–736. Springer, 2020.
- Kaicheng Yu, Tang Tao, Hongwei Xie, Zhiwei Lin, Tingting Liang, Bing Wang, Peng Chen, Dayang Hao, Yongtao Wang, and Xiaodan Liang. Benchmarking the robustness of lidar-camera fusion for 3d object detection. In *Proceedings of the IEEE/CVF Conference on Computer Vision and Pattern Recognition*, pp. 3187–3197, 2023.
- Qihang Yu, Huiyu Wang, Siyuan Qiao, Maxwell Collins, Yukun Zhu, Hartwig Adam, Alan Yuille, and Liang-Chieh Chen. k-means mask transformer. In *European Conference on Computer Vision*, pp. 288–307. Springer, 2022.
- Jianfeng Zhang, Yujun Cai, Shuicheng Yan, Jiashi Feng, et al. Direct multi-view multi-person 3d pose estimation. *Advances in Neural Information Processing Systems*, 34:13153–13164, 2021a.
- Xinyu Zhang, Zhiwei Li, Xin Gao, Dafeng Jin, and Jun Li. Channel attention in lidar-camera fusion for lane line segmentation. *Pattern Recognition*, 118:108020, 2021b.
- Tu Zheng, Hao Fang, Yi Zhang, Wenjian Tang, Zheng Yang, Haifeng Liu, and Deng Cai. Resa: Recurrent feature-shift aggregator for lane detection. In *Proceedings of the AAAI Conference on Artificial Intelligence*, volume 35, pp. 3547–3554, 2021.

Yin Zhou and Oncel Tuzel. Voxelnet: End-to-end learning for point cloud based 3d object detection.  
In *Proceedings of the IEEE conference on computer vision and pattern recognition*, pp. 4490–4499, 2018.

Xizhou Zhu, Weijie Su, Lewei Lu, Bin Li, Xiaogang Wang, and Jifeng Dai. Deformable detr: Deformable transformers for end-to-end object detection. *arXiv preprint arXiv:2010.04159*, 2020.

## A APPENDIX

### A.1 MODEL COMPLEXITY

As stated in our main paper, DV-3DLane achieves SoTA performance, and its lite version also surpasses all previous methods in terms of F1 score and localization errors, while achieving an impressive FPS of 13.49. In this section, we study the model complexity, as shown in Table 1. Our base model achieves a competitive FPS of 8.82 while maintaining a strong F1 score of 63.5. Notably, our tiny version excels with an FPS of 13.49, along with a notable F1 score of 60.9.

### A.2 SCENARIO STUDIES

Additionally, we comprehensively evaluated DV-3DLane across *diverse scenarios* within OpenLane. As depicted in Table 2, our method consistently outperforms all previous approaches across all six challenging scenarios by a large margin. Visualizations are provided in Figure 1. Overall, these results reveal the effectiveness of our design.

Table 2: Comparison with other 3D lane detection methods on the OpenLane validation dataset.  $\dagger$  denotes that the results are obtained using their provided models.

<i>Dist.</i>	<b>Methods</b>	<b>Backbone</b>	<b>Modality</b>	<b>All</b>	<b>Up &amp; Down</b>	<b>Curve</b>	<b>Extreme Weather</b>	<b>Night</b>	<b>Intersection</b>	<b>Merge &amp; Split</b>
1.5 m	3DLaneNet Garnett et al. (2019)	VGG-16	C	44.1	40.8	46.5	47.5	41.5	32.1	41.7
	GenLaneNet Guo et al. (2020)	ERFNet	C	32.3	25.4	33.5	28.1	18.7	21.4	31.0
	PersFormer Chen et al. (2022)	EffNet-B7	C	50.5	42.4	55.6	48.6	46.6	40.0	50.7
	Anchor3DLane Huang et al. (2023) $\dagger$	EffNet-B3	C	52.8	48.5	50.7	56.9	43.6	48.5	50.7
	M <sup>2</sup> -3DLaneNet Luo et al. (2022a)	EffNet-B7	C+L	55.5	53.4	60.7	56.2	51.6	43.8	51.4
	PersFormer Chen et al. (2022)	ResNet-50	C	52.7	46.4	57.9	52.9	47.2	41.6	51.4
	LATR Luo et al. (2023)	ResNet-50	C	61.9	55.2	68.2	57.1	55.4	52.3	61.5
	Anchor3DLane Huang et al. (2023) $\dagger$	ResNet-18	C	50.7	45.3	53.7	48.5	51.6	45.3	48.5
	DV-3DLane-Tiny	ResNet-18	C+L	63.4	59.9	69.8	62.2	58.8	53.5	60.6
	DV-3DLane-Base	ResNet-34	C+L	65.4	60.9	72.1	64.5	61.3	55.5	61.6
	DV-3DLane-Large	ResNet-50	C+L	<b>66.8</b>	<b>61.1</b>	71.5	<b>64.9</b>	<b>63.2</b>	<b>58.6</b>	<b>62.8</b>
0.5 m	<i>Improvement</i>		-	-	<b>↑4.9</b>	<b>↑5.9</b>	<b>↑3.9</b>	<b>↑7.8</b>	<b>↑6.3</b>	<b>↑1.3</b>
	PersFormer Chen et al. (2022)	EffNet-B7	C	36.5	26.8	36.9	33.9	34.0	28.5	37.4
	Anchor3DLane Huang et al. (2023) $\dagger$	EffNet-B3	C	34.9	28.3	31.8	30.7	32.2	29.9	33.9
	M <sup>2</sup> -3DLaneNet Luo et al. (2022a)	EffNet-B7	C+L	48.2	40.7	48.2	<b>49.8</b>	<b>46.2</b>	38.7	44.2
	PersFormer Chen et al. (2022)	ResNet-50	C	43.2	36.3	42.4	45.4	39.3	32.9	41.7
	LATR Luo et al. (2023)	ResNet-50	C	<b>54.0</b>	<b>44.9</b>	<b>56.2</b>	47.6	<b>46.2</b>	<b>45.5</b>	<b>55.6</b>
	Anchor3DLane Huang et al. (2023) $\dagger$	ResNet-18	C	32.8	26.5	27.6	31.2	30.0	28.1	31.7
	DV-3DLane-Tiny	ResNet-18	C+L	60.9	56.9	65.9	60.0	56.8	50.7	57.6
	DV-3DLane-Base	ResNet-34	C+L	63.5	58.6	<b>69.3</b>	62.4	59.9	53.9	59.3
	DV-3DLane-Large	ResNet-50	C+L	<b>65.2</b>	<b>59.1</b>	69.2	<b>63.0</b>	<b>62.0</b>	<b>56.9</b>	<b>60.5</b>
	<i>Improvement</i>		-	-	<b>↑11.2</b>	<b>↑14.2</b>	<b>↑13.1</b>	<b>↑13.2</b>	<b>↑15.8</b>	<b>↑11.4</b>

### A.3 ROBUSTNESS

To investigate the robustness of our model amid calibration noise, given that perfect calibration is not always viable in real-world settings, we conduct experiments incorporating diverse levels of calibration noise to understand the model’s performance under noisy conditions.

**Noise settings:** Following the methodology of Yu et al. (2023), we introduce two noise settings: **Noise (N)** and **Stronger Noise (SN)**. In ‘Noise (N),’ we introduce random rotations within  $[1^\circ, 5^\circ]$  and translations within  $[0.5\text{cm}, 1.0\text{cm}]$  to the calibration. For ‘Stronger Noise (SN),’ these parameters are doubled to reflect stronger calibration disturbances.

**Results without training noise:** We first test our model, which has *not* been trained with additional noise under these noisy conditions. The results, presented in the first row of Table 3, show a

Table 1: **Model complexity.** FPS is evaluated on a single V100 GPU.

<b>Model</b>	<b>Backbone</b>	<b>FPS</b>	<b>F1</b>
PersFormer	Efficient-B7	11.67	36.5
PersFormer	Res50	9.48	43.2
M <sup>2</sup> -3DLaneNet	Efficient-B7	6.48	48.2
Anchor3DLane	Efficient-B3	3.07	34.9
Anchor3DLane	Res18	3.45	32.8
LATR	Res50	13.34	54.0
DV-3DLane-Tiny	Res18, PillarNet18	13.49	60.9
DV-3DLane-Base	Res34, PillarNet34	8.82	63.5
DV-3DLane-Large	Res50, PillarNet34	6.18	65.2

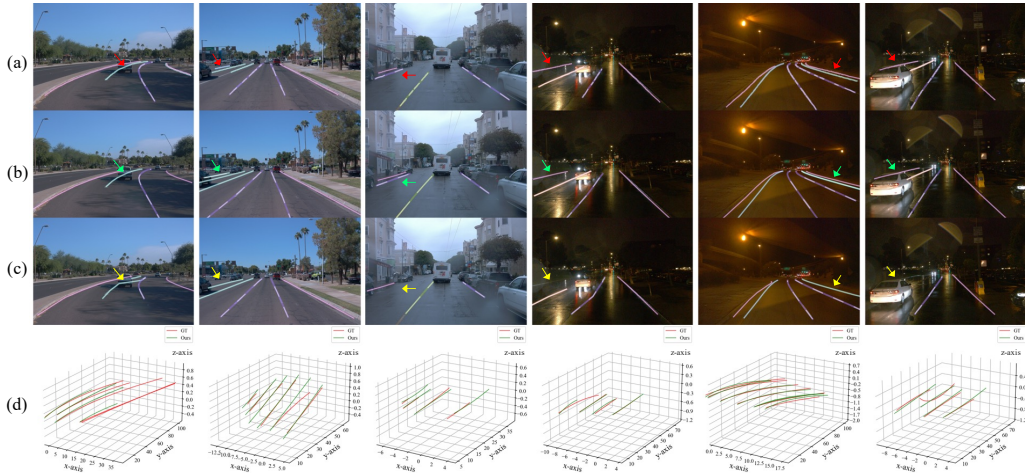


**Figure 1: More Results.** Rows (a), (b), (c) show projections of 3D lanes from the **ground truth** (GT), **DV-3DLane**, and **LATR** Luo et al. (2023), with differences highlighted by colored arrows. Row (d) compares GT (red) and our prediction (green) in 3D. Best viewed in color and zoom in for details.

notable performance decline as the noise intensity increases. Specifically, under a probability setting of 0.7, the performance deteriorates from 63.5 to 32.4/31.4 in the ‘Noise’/‘Stronger Noise’ settings.

**Enhancing robustness via training:** To enhance robustness, we incorporate calibration noise during the training phase. This strategy substantially mitigates the performance degradation caused by noisy calibration, as shown in the second and third rows of Table 3.

**Comparative analysis:** Compared to the baseline (first row), we can observe that training with calibration noise significantly strengthens the robustness of our model. It effectively maintains comparable results under noisy calibration conditions. Additionally, the model trained with ‘Stronger Noise’ exhibits greater robustness compared to the one trained with less intense noise, underscoring the benefits of this training strategy.

**Table 3: Impact of noise on calibration parameters.** We set two noise levels in the experiments, “**Noise (N)**” and “**Stronger Noise (SN)**. In the **Train** column, “-” denotes *no* noise is added during the training phase. “Prob” denotes the probability of adding the corresponding noise into the training/eval phases. Each result group consists of F1-score / Accuracy.

Train @noise (N/SN)	Eval							
	—		+ Noise (N)		+ Stronger Noise (SN)			
	Prob=0.0	Prob=0.3	Prob=0.5	Prob=0.7	Prob=0.3	Prob=0.5	Prob=0.7	
-	Prob=0.0	63.5 / 92.4	52.2 / 89.9	40.9 / 85.6	32.4 / 82.5	52.0 / 89.0	40.3 / 83.4	31.4 / 79.2
N	Prob=0.3	63.0 / 93.1	62.5 / 92.9	62.0 / 92.9	61.5 / 92.9	62.2 / 92.9	61.5 / 92.9	60.8 / 92.7
SN	Prob=0.3	63.4 / 92.5	62.8 / 92.4	62.3 / 92.3	61.8 / 92.2	62.7 / 92.4	62.1 / 92.2	61.7 / 92.2

#### A.4 EFFECT OF DUAL-VIEW

Apart from studying the impact of multiple modalities, we conducted experiments on the OpenLane-1K dataset to analyze the effect of the dual views, providing a comprehensive understanding of our approach. As shown in Table 4, we conducted two sets of experiments: **1)** Using single modality and single view. **2)** Using single modality but dual views.

In the first set of experiments, rows #1 and #2 present the performance using individual modalities.

In the second set of experiments:

- For the image branch experiment, we adopt a strategy similar to BEVFormer Li et al. (2022d), utilizing deformable attention to transform image features into BEV features.

Then, we apply our dual-view decoder upon this, and the outcomes are illustrated in row #3 of Table 4.

- For the LiDAR branch experiment, we project LiDAR point cloud features onto the 2D image plane to generate perspective-view features. The results of this approach are presented in row #4 of Table 4.

The results in Table 4 underscore that the dual-view representation significantly enhances the performance of baseline models in single-modal scenarios (comparing #1 with #3 and #2 with #4). This improvement confirms the effectiveness of our dual-view approach in learning 3D lane detection. Most notably, the combination of image and LiDAR modalities, coupled with our dual-view representation, achieves the best results, as shown in row #5. This synergy of modalities underlines the superiority of our proposed method.

Table 4: Comparison of single and dual-view approaches on OpenLane-1K dataset with 0.5m setting.

# Line	Inputs	View	Backbone	F1	Acc.	X error (m) near   far	Z error (m) near   far
#1	Image	PV	Res34	52.9	90.3	0.173   0.212	0.069   0.098
#2	LiDAR	BEV	PillarNet34	54.1	84.4	0.282   0.191	0.096   0.123
#3	Image	Dual Views	Res34	54.3	91.5	0.165   0.200	0.067   0.094
#4	LiDAR	Dual Views	PillarNet34	55.3	87.9	0.156   0.143	0.031   0.050
#5	DV-3DLane	Dual Views	Res34+PillarNet34	63.5	92.4	0.090   0.102	0.031   0.053

### A.5 EFFECT OF BIDIRECTIONAL FEATURE FUSION.

To validate the effectiveness of this strategy, we compare the performance of our method with the other three fusion design choices, as shown in Table 5, where “Cam” means only image features in PV branch, and “LiDAR” denotes only point features in BEV branch. “L→C” denotes the LiDAR to camera fusion for PV branch, and conversely, “C→L” denotes the camera to LiDAR fusion for BEV branch. It shows that the absence of fusion leads to the poorest performance (#1). Further, employing one-way fusion, either from camera to LiDAR (#2) or LiDAR to camera (#3), results in 1.2% and 1.1% improvements, respectively *w.r.t.* non-fusion (#1). Remarkably, our bidirectional fusion (#4) yields the highest performance, a 2.8% gain in F1. This improvement highlights the efficacy of our strategy in effectively leveraging multi-modal features in both PV and BEV spaces.

Table 5: Effect of bidirectional feature fusion.

# Line	Methods	F1	X error (m) near   far	Z error (m) near   far
#1	Cam & LiDAR	67.9	0.133   0.157	0.060   0.083
#2	Cam & C→L	69.1	0.135   0.151	0.060   0.081
#3	L→C & LiDAR	69.0	0.130   0.156	0.059   0.078
#4	L→C & C→L	70.7	0.123   0.146	0.058   0.078

### A.6 IMAGE BRANCH ON APOLLO

Table. 6 illustrates the results of our image branch on the Apollo dataset Guo et al. (2020), compared with existing methods.

Table 6: **Results on Apollo 3D Synthetic dataset.** “Image-Branch” denotes the image branch of our DV-3DLane.

Scene	Methods	F1 $\uparrow$	AP $\uparrow$	X error (m) $\downarrow$		Z error (m) $\downarrow$	
				near	far	near	far
Balanced Scene	3DLaneNet Garnett et al. (2019)	86.4	89.3	0.068	0.477	0.015	0.202
	Gen-LaneNet Guo et al. (2020)	88.1	90.1	0.061	0.496	0.012	0.214
	CLGo Liu et al. (2022)	91.9	94.2	0.061	0.361	0.029	0.250
	PersFormer Chen et al. (2022)	92.9	-	0.054	0.356	0.010	0.234
	GP Li et al. (2022a)	91.9	93.8	0.049	0.387	0.008	0.213
	CurveFormer Bai et al. (2022b)	95.8	97.3	0.078	0.326	0.018	0.219
	Anchor3DLane Huang et al. (2023)	95.6	97.2	0.052	0.306	0.015	0.223
	LATR Luo et al. (2023)	96.8	97.9	0.022	0.253	0.007	0.202
	Image-Branch (Ours)	96.4	97.6	0.046	0.299	0.016	0.213
Rare Subset	3DLaneNet Garnett et al. (2019)	74.6	72.0	0.166	0.855	0.039	0.521
	Gen-LaneNet Guo et al. (2020)	78.0	79.0	0.139	0.903	0.030	0.539
	CLGo Liu et al. (2022)	86.1	88.3	0.147	0.735	0.071	0.609
	PersFormer Chen et al. (2022)	87.5	-	0.107	0.782	0.024	0.602
	GP Li et al. (2022a)	83.7	85.2	0.126	0.903	0.023	0.625
	CurveFormer Bai et al. (2022b)	95.6	97.1	0.182	0.737	0.039	0.561
	Anchor3DLane Huang et al. (2023)	94.4	96.9	0.094	0.693	0.027	0.579
	LATR Luo et al. (2023)	96.1	97.3	0.050	0.600	0.015	0.532
	Image-Branch (Ours)	95.6	97.2	0.071	0.664	0.025	0.568
Visual Variations	3DLaneNet Garnett et al. (2019)	74.9	72.5	0.115	0.601	0.032	0.230
	Gen-LaneNet Guo et al. (2020)	85.3	87.2	0.074	0.538	0.015	0.232
	CLGo Liu et al. (2022)	87.3	89.2	0.084	0.464	0.045	0.312
	PersFormer Chen et al. (2022)	89.6	-	0.074	0.430	0.015	0.266
	GP Li et al. (2022a)	89.9	92.1	0.060	0.446	0.011	0.235
	CurveFormer Bai et al. (2022b)	90.8	93.0	0.125	0.410	0.028	0.254
	Anchor3DLane Huang et al. (2023)	91.4	93.6	0.068	0.367	0.020	0.232
	LATR Luo et al. (2023)	95.1	96.6	0.045	0.315	0.016	0.228
	Image-Branch (Ours)	91.3	93.4	0.095	0.417	0.040	0.320